Article

Fabrication of Protective Organic Layer Using Schiff-Base Metal Complex Responsible for Excellent Corrosion Performance: Experimental and Theoretical Perspectives

Hamid Ahchouch, Abdelkarim Chaouiki,* Aisha H. Al-Moubaraki, Jamilah M. Al-Ahmari, Azza A. Al-Ghamdi, Lahcen Bammou, M'hammed Belkhaouda, Maryam Chafiq,* and Young Gun Ko*

Read Online

ACCESS | Metrics & More | Article Recommendations

ABSTRACT: The effectiveness of a copper(II) complex with a Schiff base derived from 2-amino-4-phenyl-5-methylthiazole and salicylaldehyde (APMS) as a corrosion inhibitor for XC18 steel in an HCl solution was investigated. Experimental findings indicated a slight negative correlation between inhibition efficiencies in 1 M HCl and temperature but a positive correlation with both inhibitor concentration and immersion time, respectively. The weight loss measurement revealed that APMS achieved a maximum inhibition rate of 92.07% at 303 K. A fitting analysis demonstrated that APMS adheres to the Langmuir adsorption isotherm. The electrochemical results revealed an enhanced inhibitive performance of APMS, with the efficiency increasing as concentrations increased, ultimately reaching a peak of 94.47% at 5×10^{-3} mol L^{-1}. Potentiodynamic polarization measurements revealed that APMS acted as a mixed-type inhibitor without affecting the corrosion mechanism. Scanning electron microscopy investigations of the metal surfaces corroborated the presence of an adsorbed organic layer. Advanced theoretical calculations utilizing density functional theory and first-principles density-functional tight-binding were conducted to gain insights into the behavior of APMS on the metal surface. APMS derives its advantages from crucial inter- and intramolecular interactions, resulting in the formation of a resilient adsorption layer, in line with the experimental findings. It is found that the presence of the APMS-based inhibitor exhibits a significant synergistic corrosion inhibition effect. The current study offers a design direction for enhancing the structural characteristics of Schiff base metal complexes, laying the groundwork for multifunctional frameworks to minimize corrosion rates with considerations for real-world use and cost-efficiency. The ability to replace harmful, expensive constituents with sustainable, and cost-effective organic alternatives represents a significant outcome of this study.
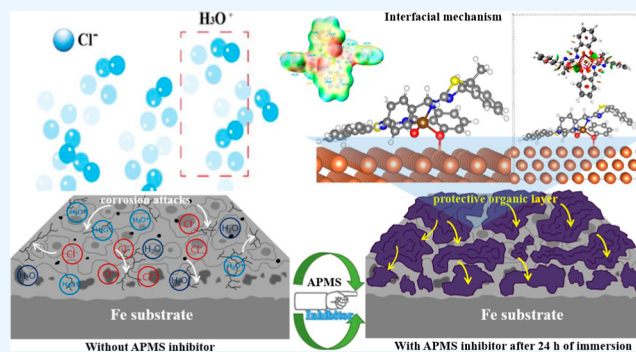
1. INTRODUCTION

Mild steel, a type of carbon steel (CS), is widely utilized in diverse industries for mechanical and structural applications. Its common use as a fabrication material extends to the chemical and petrochemical industries. Additionally, mild steel serves as a key structural engineering material, employed in significant quantities in marine engineering, petroleum pipelines, and construction in the mining industry due to its favorable mechanical properties and cost effectiveness.[1] One specific type of CS, XC18, is widely employed. Nevertheless, the corrosion of XC18 raises major concerns because of its susceptibility to corrosion and its wide array of uses.[2] Diluted acidic solutions are commonly used for various applications, including metal surface preparation, sanitizing industrial machinery, removing mineral deposits through acidification, and acidizing oil wells, all of which can cause significant corrosion in iron and steel.[3] These tasks come with the disadvantage that the intense acidic exposure dissolves the metal, resulting in defects or potentially inducing permanent structural weakness in essential machine elements.[4] As a result of the substantial financial losses and security risks stemming from corrosion in numerous industrial domains, safeguarding metal structures has garnered significant focus. Consequently, because of its susceptibility to corrosion, innovative methods must be developed to shield steel from the effects of corrosion.

A widely adopted approach to combating acid-induced corrosion is with organic inhibitors. Numerous molecules containing heteroatoms (such as N, S, and O atoms), double

bonds, and aromatic groups have demonstrated exceptional anticorrosion properties due to their free electron pairs that provide them the ability to be adsorbed and establish a protective film on the metal surface.[5] Schiff bases (SB) are a prominent class of organic compounds arising from the condensation reaction between an active carbonyl group and a primary amine. The exploration and understanding of their chemistry can be attributed to the pioneering efforts of German chemist Hugo Schiff in 1864. This pivotal discovery marked a revolutionary advancement within the realm of coordination chemistry during the late 19th century.[6] Currently, SB plays a crucial role in coordination chemistry, standing out as a preferred option for creating chemical frameworks. Their important role is due to the simplicity of synthesis, diverse properties, and various applications in biomedical, biochemical, and industrial contexts.[7] In this context, Schiff bases, among organic inhibitors, have undergone extensive research as acid corrosion inhibitors for metallic surfaces. These SB, identified through the existence of a functional imine (−N═CH) group, have garnered significant attention from researchers and are the products of the interaction between aldehydes or ketones and primary amines[8] because of the bioactive azomethine core they contain.[9] The wide range of structures available and the relatively simple process of synthesizing SB and its metallic complexes have positioned them as potential choices for corrosion prevention. Among the numerous benefits of an ideal inhibitor are its high inhibitory effectiveness, affordability, minimal toxicity, and ease of production.[10] Several SB compounds have been investigated, and these have demonstrated effective inhibition properties for metals and alloys in acidic environments.[11] SB have been utilized in the synthesis of metal complexes, owing to their ease of manufacture and their strong affinity for binding with metals. Existing research largely overlooks the potential of SB and their metal complexes as corrosion inhibitors for steel in acidic solutions.[12] Various SB and their metallic complexes have demonstrated their effectiveness in effectively preventing the corrosion of steel in acidic environments.[10,13] Arshad et al. studied the anticorrosive potential of synthesized melamine−isatin tris Schiff bases for mild steel in 0.5 M HCl. The maximum inhibitory efficiency (92.07%) was obtained at a concentration of 42.80×10^{-3} mM.[14] Abdelmaksoud et al. investigated the anticorrosive potential of two organic inhibitors prepared via SB for CS in a 2 M HCl solution; the highest inhibition efficiency observed was 95.56% at a concentration of 150 ppm.[15] Liu et al. explored the effect of the bis-thiophene Schiff base copper−metal complex on the Q235 CS in 1 M HCl. The corrosion inhibition efficiency reached a maximum of 95.2% at 100 ppm.[16] In another recent study, Thabet et al. discussed the potential for corrosion inhibition of three SBs for CS in 1 M HCl. The inhibitory performance achieved 93% at a concentration of 250 ppm.[17] In their study, Zobeidi et al. synthesized three compounds derived from SBs to explore their ability to inhibit acid corrosion of XC70 steel in 1 M HCl. The results indicated that the highest degree of inhibition observed at a concentration of 6×10^{-5} M, was 87.27%.[18]

Metal complexes of SBs containing heterocyclic compounds are also utilized for their potential applications in drug development.[19] Abd-Elzaher et al. prepared an SB ligand from salicylaldehyde with 2-amino-4-phenyl-5-methyl thiazole. This ligand was then employed for the synthesis of complexes with Cu(II), Ni(II), Co(II), and Zn(II). The research

demonstrated that the Zn(II) complex exhibited anticancer activity.[19] In a continuing effort to find more applications for metal complexes of SBs, the objective herein is to evaluate the anticorrosion activity of the copper(II) complex of SB derived from 2-amino-4-phenyl-5-methyl thiazole with salicylaldehyde (APMS) against corrosion of XC18 steel in 1 M HCl medium. To the best of our knowledge, there is no documented evidence of XC18 steel surface protection using the APMS compound in a 1 M HCl medium. For this target, the main aim of this study is to bridge the current knowledge gap by conducting a comprehensive examination and clarification of the corrosion inhibitory effectiveness, along with the interfacial mechanism behavior, of the APMS inhibitor. The APMS inhibitor was meticulously prepared using the general procedure described elsewhere.[19] Briefly, salicylaldehyde and 2-amino-4-phenyl-5-methyl thiazole were subjected to a condensation reaction in an ethanol solution with the addition of a few drops of glacial acetic acid, yielding a Schiff base ligand. Subsequently, this ligand was employed for the synthesis of a copper (Cu) complex through reaction with $CuCl_2 \cdot 2H_2O$ under reflux conditions in ethanol. This synthetic approach serves as a robust foundation for the preparation of the APMS-based inhibitor. The choice of precursor compounds and the specific reaction conditions contribute to the unique molecular structure of the inhibitor, rendering it a promising candidate for corrosion inhibition of XC18 steel in HCl solution. The objective is to advocate for the development of corrosion inhibitors that possess environmentally friendly characteristics, distinguished by their effectiveness and minimal toxicity impact. Hence, the electrochemical performance and active anticorrosion characteristics of APMS as an XC18 corrosion inhibitor were studied using various electrochemical and microscopic surface morphology techniques, including the mass loss (ML) method, electrochemical impedance spectroscopy (EIS), potentiodynamic polarization measurement (PDP), and scanning electron microscopy (SEM). Moreover, further understanding of the synergistic mechanism and interfacial adsorption behavior of the investigated compound on the Fe(110) surface has been elucidated through quantum chemistry calculations. Corresponding electronic properties were examined using the density functional theory (DFT) method and first-principles density-functional tight-binding (DFTB) calculations, which aim to understand how the donor−acceptor character of the inhibitor can influence its adsorption ability. Theoretical calculations were carried out to assess the electrostatic potential (ESP) on the molecular van der Waals (vdW) surface and to analyze the reduced density gradient (RDG). These calculations aimed to predict reactive sites and investigate both inter- and intramolecular interactions. This involves estimating the adsorption and binding of the compound on the XC18 steel surface. The investigation demonstrated that the APMS compound demonstrated a significant level of reactivity with the metallic surface, triggering the formation of strong bonding and promoting the development of a protective film with uniform distribution and efficient corrosion performance. This can be attributed to the outstanding donor−acceptor properties of the APMS, as well as the combined effects resulting from inter- and intramolecular interactions surrounding the active sites.

2. MATERIAL AND METHODS

2.1. Material and Solution Preparation. A plate of XC18 steel with the chemical composition (weight %), C =

0.18%, P = 0.05%, Mn = 0.05%, Si = 0.16%, S ≤ 0.035%, and Fe ≈ 99.5, was used as the substrate. Hydrochloric acid solutions were prepared by diluting 37% HCl (Sigma-Aldrich, ACS grade) with distilled water. XC18 plates with defined surfaces and treated in advance were used for both WL tests and surface analysis. The electrochemical tests are conducted by using a standard three-electrode Pyrex cell setup. Each XC18 sample underwent mechanical polishing using emery paper with increasingly finer grades, including papers with grades of 800, 1000, 1200, and 1600. Prior to immersion in the test solution, the XC18 samples were subjected to a cleaning process. Initially, they were cleaned using distilled water, after which they underwent degreasing with acetone (99.5%, Sigma-Aldrich), and finally, they were dried using ambient air. The effectiveness of APMS on XC18 in 1 M HCl is investigated by examining different concentrations, ranging from 1×10^{-4} to 5×10^{-3} mol/L.

2.2. Weight Loss (WL) Study. The assessment of WL provides a fundamental means of investigating the metal corrosion rate in either an inhibited or uninhibited electrolytic solution. The pretreated rectangular XC18 plates (0.1 × 1.5 × 1.5 cm) were weighed accurately and submerged in 100 mL of a 1 M HCl solution for a duration of 24 h. After each experiment, the XC18 steel plates were extracted from the assay medium, the corrosion products were eliminated, and they were washed with distilled water and ethanol before undergoing drying, after which they were precisely weighed again. Three separate tests under the same conditions were run, and the standard deviation was computed. All measurements were independently performed three times for the sake of reliability. To examine the impact of temperature on the thermodynamic activation parameters, the tests were carried out at various temperatures, ranging from 303 to 333 K. Corrosion rate (ϑ_{WL}), inhibition efficiency, and surface coverage (θ) were determined using eqs 1−3, as described below[20]

$$\vartheta_{WL} = \frac{w_1 - w_2}{S \times t} \tag{1}$$

$$\eta_{WL}(\%) = \frac{\vartheta^0_{WL} - \vartheta_{WL}}{\vartheta^0_{WL}} \times 100 \tag{2}$$

$$\theta = \frac{\nu^o_{WL} - \vartheta_{WL}}{\nu^o_{WL}} \tag{3}$$

where w_1 and w_2 represent the mass of the XC18 before and after immersion in different concentrations of APMS, respectively. S denotes the surface area of the XC18 plate in cm^2, and t represents the immersion time in hours (h). The symbols ϑ_{WL} and ϑ_{WL}^0 refer to the corrosion rate of XC18 with the addition of APMS and in the absence of APMS, respectively.

2.3. Electrochemical Evaluations. For the electrochemical study, a potentiostat/galvanostat obtained from Corrtest Instruments Corp. Ltd. (Hubei, China) was employed. The potential was measured with respect to a saturated calomel reference electrode (SCE). The counter electrode consisted of a platinum sheet. The working electrode, made of XC18 steel, had a rectangular shape with a surface area of 0.14 cm^2 in contact with the corrosive solution. Prior to the study, the working electrode surface was smoothed using abrasive papers of different-sized grains. Each trial was carried

out at a constant temperature of (303 ± 0.5) K. The working electrode was submerged in the 1 M HCl medium for a period of 30 min to allow for the steadiness of the open circuit potential (OCP). Subsequently, electrochemical tests were performed. EIS measurements were conducted over a frequency range spanning from 10^5 to 10^{-2} Hz and an amplitude of 10^{-2} V. For PDP, the electrode potential was swept at a rate of 1.0 mV/s, ranging from −700 to −300 mV vs SCE, to generate Tafel plots. The estimated parameters' values presented in the results are the mean of three separate tests conducted under similar conditions.

2.4. Surface Roughness Analyses. As mentioned previously, the treated XC18 samples were subjected to 48 h exposure to an acidic medium. This exposure was achieved by immersing the samples in 50 mL of a 1.0 M HCl solution with and without the addition of 5×10^{-3} M of APMS inhibitor at room temperature. Subsequently, the samples were meticulously extracted, rinsed with purified water, and desiccated using a vacuum. The morphology of the surface was analyzed using SEM with a Hitachi S-4800 instrument.[21,22]

2.5. Theoretical Calculations. To enhance comprehension of the mechanism at the molecular level responsible for corrosion inhibition, it is essential to explore the quantum chemical characteristics and interfacial interactions of the APMS/XC18 combination. By doing so, valuable insights into adsorption phenomena and their electronic effects can be obtained. To accomplish this, several theoretical chemistry calculations, such as DFT, ESP, ESP colored vdW surface, RDG analyses, and DFTB simulations, were utilized to analyze and establish correlations between the molecular characteristics of the APMS and its adsorption mechanism. The Gaussian 16 W software was employed for modeling and optimizing the molecular configuration and electronic stability of the molecule in the aqueous phase, utilizing the SMD model. The functional B3LYP/6-311G++(d,p) was chosen for the ground-state computation. To validate experimental observations, different overall reactivity properties were computed, including electron affinity (A), ionization potential (I), electronegativity (χ), hardness (η), softness (σ), electrophilicity (ω), and fraction of transferred electrons (ΔN). These calculations were based on the highest occupied molecular orbital energy (HOMO), lowest unoccupied molecular orbital energy (LUMO), and energy gap (ΔE). For further details on the simulation process, readers can refer to the works by Chaouiki et al.[23−25]

The following formula was used to predict the interaction between the inhibitor compound and the metal interface during the corrosive process[26,27]

$$E_{interaction} = E_{total} - (E_{surf+sol} + E_{inhibitor}) \tag{4}$$

where E_{total} represents the calculated total energy of the system through simulation, $E_{surf+sol}$ denotes the energy calculated for the system iron/solution, and $E_{inhibitor}$ is the total energy of the inhibitor alone.

Additionally, the formula below was used to quantitatively describe the binding energy during the corrosive process

$$E_{interaction} = -E_{binding} \tag{5}$$

3. RESULTS AND DISCUSSION

3.1. WL Measurements. *3.1.1. Concentration Dependence.* The WL analysis was conducted at various concen-

trations of APMS, and the results are presented in Figure 1. The inhibited system exhibited significantly lower corrosion
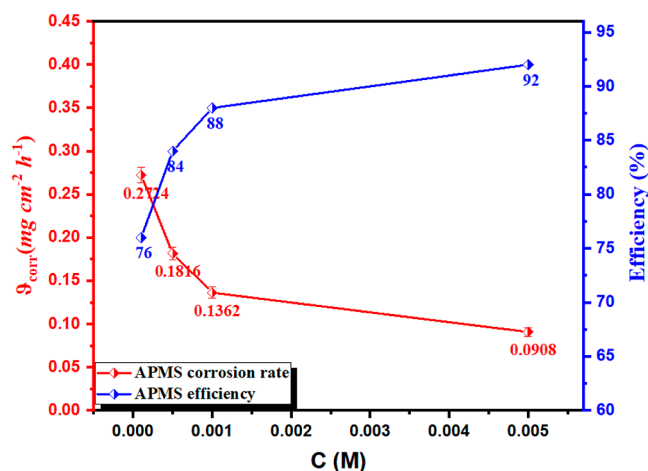

Figure 1. Impact of APMS concentration on both corrosion rate and inhibition efficiency using the WL method at 303 K.

Table 1. Influence of APMS Concentration and Temperature on the Corrosion Rate and Inhibition Efficiency of XC18 Steel in 1.0 M HCl Solution

	concentration (mol L^{-1})	temperature (K)	ϑ_{WL} (mg cm^{-2} h^{-1})	η_{WL}
blank	1.0 M HCl	303 ± 0.5	1.1351 ± 0.0012	–
		313 ± 0.5	1.4160 ± 0.0017	–
		323 ± 0.5	1.9980 ± 0.0013	–
		333 ± 0.5	2.5391 ± 0.0014	–
APMS	5 × 10^{-3}	303 ± 0.5	0.0908 ± 0.0002	92.07
		313 ± 0.5	0.1416 ± 0.0003	90.04
		323 ± 0.5	0.2597 ± 0.0003	87.03
		333 ± 0.5	0.4062 ± 0.0008	84.00
	1 × 10^{-3}	303 ± 0.5	0.1362 ± 0.0003	88.01
		313 ± 0.5	0.1982 ± 0.0004	86.01
		323 ± 0.5	0.3596 ± 0.0007	82.03
		333 ± 0.5	0.5332 ± 0.0010	78.99
	5 × 10^{-4}	303 ± 0.5	0.1816 ± 0.0004	84.00
		313 ± 0.5	0.2407 ± 0.0005	83.10
		323 ± 0.5	0.4196 ± 0.0008	79.03
		333 ± 0.5	0.6094 ± 0.0012	76.01
	1 × 10^{-4}	303 ± 0.5	0.2724 ± 0.0005	76.04
		313 ± 0.5	0.3682 ± 0.0007	73.94
		323 ± 0.5	0.5794 ± 0.0011	70.97
		333 ± 0.5	0.8125 ± 0.0016	67.98

rate (ϑ_{corr}) values compared with the uninhibited medium. Moreover, increasing APMS concentration results in a significant reduction in the rate of corrosion. Regarding XC18, ϑ_{corr} decreases from 0.272 mg cm^{-2} h^{-1} in a solution with a concentration of 1×10^{-4} M of APMS to 0.090 mg cm^{-2} h^{-1} in the presence of 5×10^{-3} mol L^{-1} APMS. The observed reduction in the corrosion rate (ϑ_{corr}) may be attributed to the adsorption of APMS onto the substrate surface, leading to the formation of a protective inhibitor layer at the electrode interface. The presence of this adsorbed layer acts as a barrier, effectively blocking corrosive ions from accessing the XC18 surface. The increasing protection efficacy observed experimentally (Figure 1) with higher APMS doses highlights the significance of the cumulative amount of adsorbed inhibitor at the electrode interface. At the optimum dose (5×10^{-3} M), the inhibitor demonstrated an optimal protection capacity of over 92.07%.

3.1.2. Temperature Dependence. Table 1 presents the correlation between the variation in corrosion rate and the effectiveness of inhibition, derived from the WL data for the investigated APMS. To study the temperature effect, a range of (303−333) K was employed to assess its impact on the efficiency of the corrosion inhibition process. Temperature is a crucial factor that influences the rate of chemical reactions, and in this context, it is believed to amplify the corrosion phenomenon. Using the same principles as observed in any typical chemical reaction, elevating the temperature boosts the thermal energy of molecules, thereby enhancing the probability of productive collisions between reactants. Similarly, if this chemical reaction accelerates, it is anticipated that the corrosion phenomenon will also be impacted accordingly.[28] With an increase in the frequency of effective collisions between the corroding steel and the different components of the corrosive solution, one can anticipate a corresponding increase in the corrosion rate. An analysis of Table 1 reveals that with increasing temperature, the corrosion process accelerates, while the inhibition efficiency shows a slight decrease. This observation can be attributed to the desorption of APMS from the XC18 surface as temperatures increase.[29]

This behavior remains consistent across all concentrations of the APMS tested.

3.2. Thermodynamic and Kinetic Parameters. Eqs 6 and 7, representing the Arrhenius-type and transition-state equations, respectively, serve as the foundation for exploring the interplay between various activation energies and the resulting corrosion rate in a corrosion process[30]

$$\vartheta_{corr} = A \exp\left(-\frac{E_a}{RT}\right) \tag{6}$$

$$v_{corr} = \frac{RT}{Nh} \exp\left(\frac{\Delta S^*}{R}\right) \exp\left(-\frac{\Delta H^*}{RT}\right) \tag{7}$$

where ΔS^* is the activation energy of entropy, ΔH^* is the activation energy of enthalpy, E_a is the apparent activation energy, T is the temperature, R is the gas constant, A is a pre-exponential factor, N is Avogadro's number, and h is Planck's constant.

Figure 2 illustrates the Arrhenius-type and transition-state plots obtained in the addition of various concentrations of APMS in a 1.0 M HCl solution. Through linear regression analysis on $\ln(v_{corr})$ and $\ln\left(\frac{\vartheta_{corr}}{T}\right)$ as functions of 1000/T, the values of E_a, ΔH^*, and ΔS^* were extracted. These various calculated parameters are summarized in Table 2. To determine the values of E_a, the slope of $\ln(v_{corr}) = f\left(\frac{1000}{T}\right)$ was multiplied by the gas constant, R.[30]

The E_a obtained in the presence of APMS is higher compared to that obtained with the blank solution. This suggests that a reaction takes place on the XC18 steel surface following the application of the APMS inhibitor.[31] The value of E_a is greater in the case of the studied inhibitor compared with the blank solution. It rises with an increase in inhibitor concentration, indicating a reduction in metal dissolution as a result of the increased activation energy barrier required for the
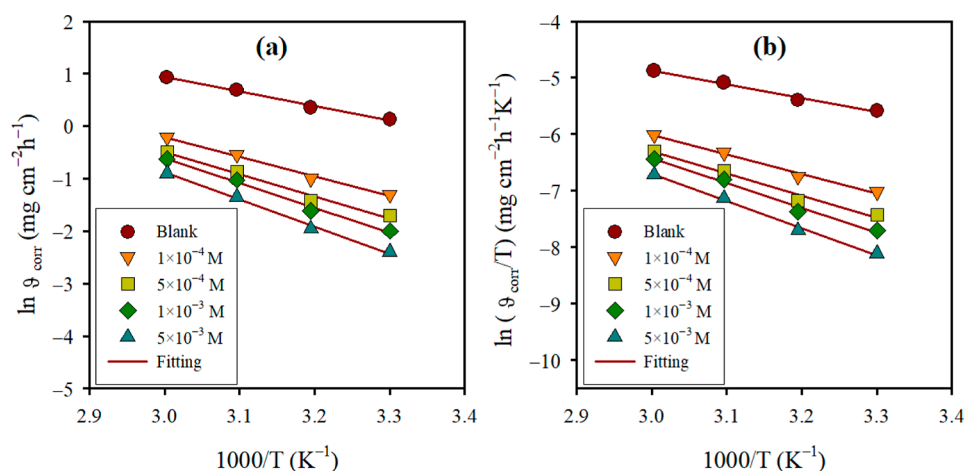
Figure 2. Temperature dependence of the corrosion rate for XC18 steel in 1.0 M HCl solution without and with various concentrations of APMS, represented by (a) Arrhenius plots and (b) transition-state plots.

**Table 2. Comparison of Activation Parameters for XC18 Steel with and without Varying Concentrations of APMS**

	blank HCl 1 mol/L	APMS (M)			
		1×10^{-4}	5×10^{-4}	1×10^{-3}	5×10^{-3}
E_a (kJ mol^{-1})	23.13	31.31	35.14	39.33	42.64
ΔH^* (kJ mol^{-1})	20.49	28.67	32.50	36.69	40.00
ΔS^*	−176.58	−161.50	−152.48	−140.87	−133.19
$E_a - \Delta H^*$ (kJ mol^{-1})	2.64	2.64	2.64	2.64	2.64

corrosion process to take place. In other words, the inhibitors raise the energy threshold required for corrosion, leading to a more effective inhibition of the metal's corrosion rate. Thus, there is a progressive decrease in the rate of transition-state complex formation.[32] The positive sign of ΔH^* indicates the endothermic nature of the corrosion reaction in 1 M HCl. It is worth noting that the disparity between E_a and ΔH^* remains roughly constant for all investigated systems, with an average value equivalent to RT in line with eq 7. This suggests that the corrosion of the XC18 steel follows a unimolecular reaction.

$$E_a - \Delta H^* = RT \tag{8}$$

Both inhibited and uninhibited solutions exhibit negative activation entropy (ΔS^*), and it may be inferred that disorder is diminished when the reactant changes into the activated complex at the upper energy barrier (i.e., the transition-state complex). As a result, association rather than dissociation is more suggestive of the active complex.[33]

3.3. Analysis of Adsorption Isotherms for APMS/ XC18. Good corrosion inhibitors exhibit the ability to strongly adhere to the metal surface via a combination of chemical and physical mechanisms. Chemisorption of the inhibitor involves the donation of lone electron pairs from its heteroatoms to empty d-orbitals of the transition metal, whereas physisorption is attributed to the electrostatic influence. During this process, the inhibitor molecules displace the H_2O molecules present on the metal surface. The summarized process is as follows[34]

$$\text{Inhibitor}_{sol} + x\text{H}_2\text{O}_{ads} \leftrightarrow \text{Inhibitor}_{ads} + x\text{H}_2\text{O}_{sol} \tag{9}$$
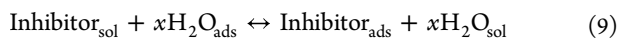
Adsorption isotherms allow for quantitative assessment of inhibitor adsorption on the metal surface. That can be employed to investigate the adherence of APMS to the surface of XC18. According to Figure 3, the adsorption of APMS molecules on the surface obeys the Langmuir isotherm model. Furthermore, the outcomes obtained from WL measurements were fitted using various other models, including Temkin, Flory−Huggins, and Freundlich, Figure 3. The coefficient of determination (R^2) was found to be close to one. The equations utilized for the adsorption isotherm models are as follows

$$\text{Langmuir:} \quad \frac{C_{inh}}{\theta} = \frac{1}{K_{ads}} + C_{inh} \tag{10}$$

$$\text{Temkin:} \quad \theta = -\frac{2.303}{2a}\log K_{ads} - \frac{2.303}{2a}\log C_{inh} \tag{11}$$

$$\text{Freundlich:} \quad \log \theta = \frac{1}{n}\log C_{inh} + \log K_{ads} \tag{12}$$

$$\text{Flory} - \text{Huggins} \log \frac{\theta}{C_{inh}} = \log K_{ads} + x\log(1 - \theta) \tag{13}$$

K_{ads} represents the adsorption equilibrium constant, while a denotes the Frumkin lateral interaction factor, which captures the impact of interactions among adsorbed molecules within the surface layer. n is a coefficient characterizing the deviation from linearity to the Langmuir isotherm, reflecting the nonequivalence of adsorption sites and the variation in the number of water molecules displaced from the adsorption layer. The variable x signifies the quantity of water molecules replaced with one inhibitor molecule. The concentration of APMS is represented by C_{inh}, and the surface fraction covered by APMS is indicated by θ.

The WL data was analyzed using the mentioned models, and Figure 3 shows the obtained results. Since the R^2 value is close to 1, the Langmuir adsorption isotherm model was chosen as the most appropriate one for describing the adsorption mechanism. As illustrated in Figure 4, the slopes and R^2 values for APMS are in very close proximity to 1. This strongly supports the validity of the Langmuir adsorption model. From eqs 10 and 15, the thermodynamic adsorption parameters (ΔG_{ads}^0 and K_{ads}) were determined at 5×10^{-3} mol
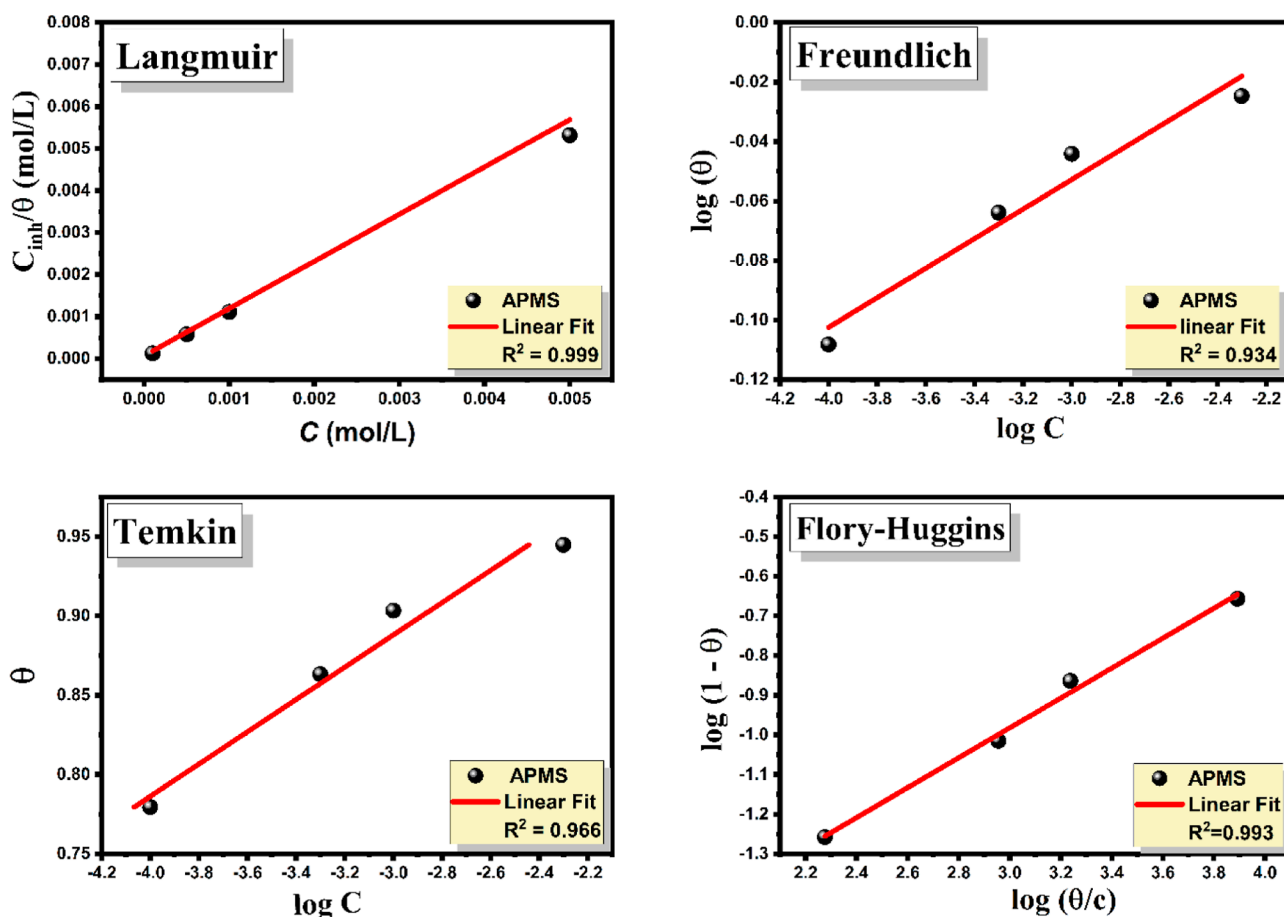
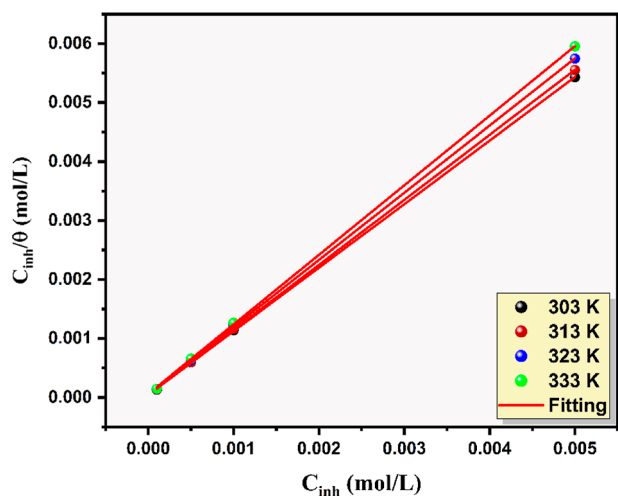**Figure 3.** Fit of θ values from different APMS concentrations to diverse adsorption isotherm models.

Figure 4. Langmuir adsorption isotherms of APMS at various temperatures.

Table 3. Langmuir's Adsorption Parameters for APMS Inhibitor in 1.0 M HCl on XC18 Steel at Different Temperatures

inhibitor	temperature (K)	K_{ads} (M^{-1})	ΔG_{ads}^0 (kJ/mol)	R^2
APMS	303	2.30×10^3	−29.60	0.999
	313	1.80×10^3	−29.94	0.999
	323	1.34×10^3	−30.10	0.999
	333	1.05×10^3	−30.36	0.999

Eq 14 depicts the adsorption process,[5] and eq 15 can be utilized for computing the Gibbs free energy.[35]

$$K_{ads} = \frac{1}{C_{H_2O}}\exp\left(-\frac{\Delta G_{ads}^0}{RT}\right) \tag{14}$$

$$\Delta G_{ads}^0 = -RT\ln(55.5 \times K_{ads}) \tag{15}$$

In the context provided, C_{H_2O} represents the concentration of H_2O, which is 55.5 M. R stands for the molar gas constant (8.314 J mol^{-1} K^{-1}), T represents the absolute temperature, and K_{ads} is calculated from the Langmuir equation.

With rising temperature (from 303 to 333 K), the adsorption of inhibitor molecules on the XC18 surface diminishes, as evidenced by the declining K_{ads} (from 2.31×10^3 to 1.05×10^3 L mol^{-1}). This implies that at elevated temperatures, inhibitor molecules are more prone to desorption from the surface. The ΔG_{ads}^0 values, spanning from −40 to −20 kJ/mol, suggest the presence of both physical

L^{-1} in a 1 M HCl solution within the temperature range of 303 to 323 K and are listed in Table 3. Gibbs free energy (ΔG_{ads}^0) can help ascertain the adsorption behavior, whether it is physisorption or chemisorption. If ΔG_{ads}^0 is below −40 kJ/mol, it indicates chemisorption. On the other hand, a value above −20 kJ/mol suggests physisorption. ΔG_{ads}^0 values falling between −40 and −20 kJ/mol are classified as mixed adsorption.[5]

and chemical adsorption mechanisms in the binding of APMS molecules to the XC18 steel surface.

3.4. Electrochemical Investigations. *3.4.1. OCP Observation.* The OCP provides valuable insights into the thermodynamic tendencies of the corrosion process. OCP varies over time due to shifts in the surface's oxidation propensity.[37] Figure 5 displays the evolution of the OCP for
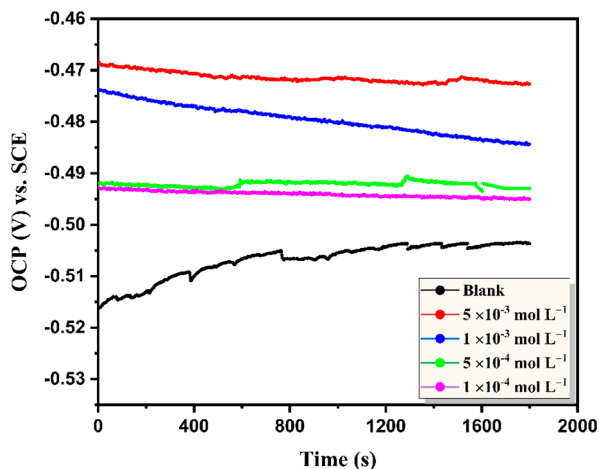

Figure 5. Effect of APMS Concentrations on the OCP of XC18 steel in 1 M HCl.

the XC18 steel in a 1 M HCl solution under varying concentrations of APMS, as well as in its absence. The OCP of the XC18 typically stabilized into a steady-state condition within the initial 1600 s following immersion in the test solutions. The variations in OCP values within the first 1600 s can be ascribed to the dynamic competition between inhibitor adsorption and desorption processes on the surface of the XC18.[38] With an increase in the APMS concentration within the range of 1×10^{-4} to 5×10^{-3} M, the OCP value exhibits a gradual rise from −492.7 to −468.2 mV vs SCE. The observed positive shift in the OCP can be ascribed to the adsorption of inhibitor molecules onto the XC18 surface.[38] Under the OCP conditions, anodic reactions such as iron oxidation are thought to be able to slow down in the presence of APMS.

3.4.2. PDP Measurements. To study the effect of APMS on XC18 steel anodic dissolution and cathodic hydrogen reduction in a 1 M HCl solution, potentiodynamic polarization tests were performed. The experimental results are presented in Figure 6, showcasing the polarization plots. The examination of these PDP curves yields several potential kinetic parameters, including corrosion current densities (i_{corr}), corrosion potential (E_{corr}), inhibition effectiveness (η), anode Tafel slope (β_a), and cathode Tafel slope (β_c), which were determined and are summarized in Table 4. Based on the PDP measurements, the corrosion inhibition efficiency ($\eta_{PDP}(\%)$) was evaluated using the following equation

$$\eta_{PDP}(\%) = \frac{i_{corr}^0 - i_{corr}^i}{i_{corr}^0} \times 100 \qquad (16)$$

where i_{corr}^0 and i_{corr}^i are the corrosion current density without and with the presence of the APMS inhibitor, respectively.

Table 4 shows that for all of the investigated concentrations, the inclusion of APMS results in a notable decrease in the corrosion current density (i_{corr}). This observed decrease in i_{corr} implies that the addition of APMS obstructed the corrosive
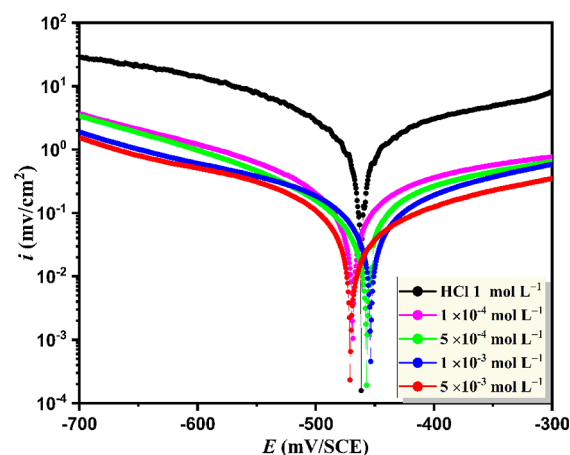

Figure 6. PDP curves of XC18 steel without and with different APMS concentrations in a 1.0 M HCl solution.

action on the steel surface by adsorbing the APMS molecules onto the active sites of the XC18 steel surface and prevented iron dissolution. Therefore, APMS demonstrated significant corrosion inhibition activity for XC18 steel. Based on the information from Figure 6, both the anodic and cathodic curves shift toward a decreasing i_{corr} direction. Additionally, the addition of APMS causes a shift in the corrosion potential (E_{corr}) toward the positive side (Table 4).

There are two primary reasons the inhibitor under investigation is classified as a mixed-type inhibitor. First, it appears that the tested APMS is affecting both cathodic and anodic reactions based on the observed shifting of both anodic and cathodic Tafel traces toward reduced i_{corr} in Figure 6. Second, there is less than an 85 mV difference in E_{corr} between the blank solution and solutions with different doses of APMS. These outcomes validate the consistency and reliability of the collected data and are in line with the conclusions from the WL measurements.[39]

3.4.3. EIS Investigation. *3.4.3.1. Concentration Effect.* The EIS technique enables the investigation of alterations taking place at the electrode interface induced by corrosion inhibitors. The in situ and nondestructive nature of EIS measurements sets it apart from other electrochemical techniques. Figure 7a shows the Nyquist plot, while Figure 7b presents the Bode plot for the XC18 steel electrode. These plots display the interface's behavior under two conditions: in the blank solution and at different concentrations of APMS. To analyze the results, a circuit comprising electrolyte resistance (R_s) and a constant phase element (CPE) in parallel with a charge-transfer resistance (R_{ct}) was used for fitting EIS data (see Figure 8). Upon observation of the Nyquist plots shown in Figure 7a, it is evident that they exhibit a virtual depressed semicircle shape, where the diameter corresponds to the R_{ct}. The inhibition proportion can be calculated by employing R_{ct}, as indicated below[40]

$$\eta_{EIS}(\%) = \frac{R_{ct}^i - R_{ct}^0}{R_{ct}^i} \times 100 \qquad (17)$$

R_{ct}^0 and R_{ct}^i are the charge-transfer resistance without and with APMS, respectively.

Various EIS parameters that result from fitting the experimental data with the proposed electrochemical equivalent circuit (Figure 8) are tabulated in Table 5. The small

Table 4. PDP Parameters for XC18 Steel in 1.0 M HCl without and with Various Concentrations of the APMS Inhibitor at 303 K

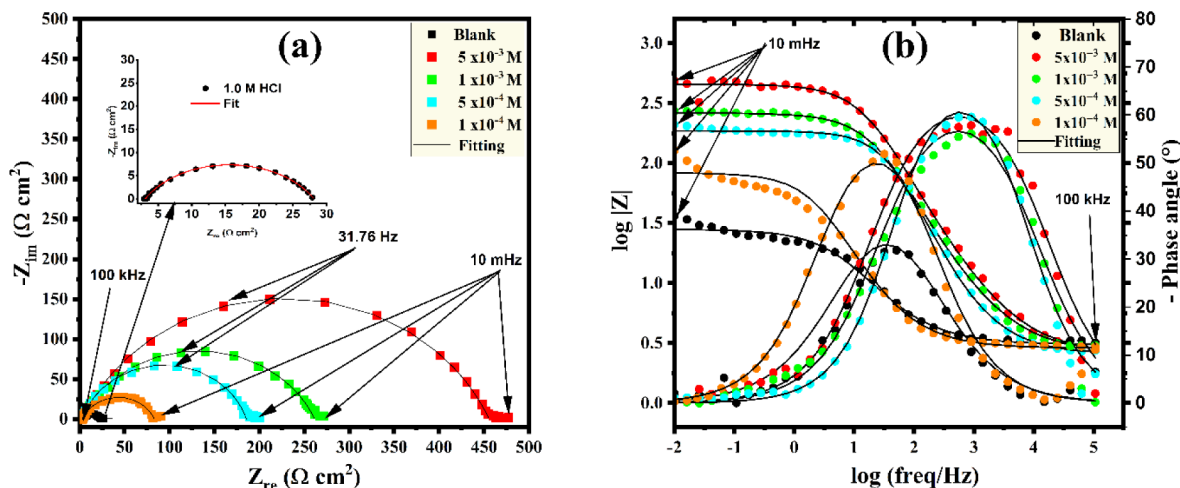| inhibitor	concentration (mol L^{-1})	$-E_{corr}$ (mV vs SCE)	$-\beta_c$ (mV dec^{-1})	i_{corr} (μA cm^{-2})	η_{PDP} (%)
blank	1.0	461.1 ± 0.3	140.1 ± 2.5	599.8 ± 0.6	–
APMS	1 × 10^{-4}	468.2 ± 0.4	160.3 ± 2.1	137.7 ± 0.5	77.03
	5 × 10^{-4}	456.5 ± 0.6	185.9 ± 1.8	89.3 ± 0.1	85.10
	1 × 10^{-3}	453.4 ± 0.4	173.2 ± 1.9	65.6 ± 0.5	89.05
	5 × 10^{-3}	471.6 ± 0.1	180.4 ± 2.2	41.9 ± 0.4	93.01

Figure 7. (a) Nyquist and (b) Bode curves of XC18 in 1.0 M HCl solution at 303 K without and with varying concentrations of the APMS inhibitor.
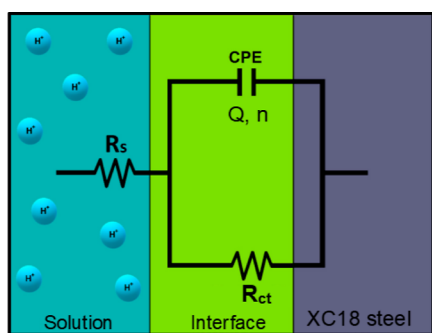

Figure 8. Equivalent circuit model used for fitting the EIS results.

value of χ_2 in Table 5 indicates the reasonableness and validity of the employed equivalent electrical circuit. The Nyquist and Bode plots display similar shapes at different concentrations, which are characterized by single capacitive loops. However, the diameter and height of the loop vary, indicating that the charge-transfer process is the predominant factor governing the dissolution of XC18 in the HCl medium. Meanwhile, the corrosion mechanism remains unaffected by the varying concentrations.[41] As the concentration increases, higher peaks and diameters are observed, suggesting more resistance

against corrosion. This phenomenon can be attributed to the APMS molecules that form a protective layer on the XC18 surface, leading to a reduced corrosion rate in the HCl solution. The Nyquist plots obtained are not perfectly semicircular. This deviation from a perfect semicircular shape can be ascribed to the inhomogeneity or surface irregularity of the metal.[42] The system cannot be fully explained by considering only C_{dl} (double-layer capacitance). However, replacing C_{dl} with CPE resolves this issue and provides a more accurate description of the electrochemical system. The relationship employed to calculate the impedance of the double-layer (Z_{CPE}) and the C_{dl} in circuits incorporating CPE is as follows[43,44]

$$Z_{CPE} = \frac{1}{Q(j\omega)^n} \tag{18}$$

$$C_{dl} = Q(\omega_{max})^{n-1} \tag{19}$$

Q represents the CPE value, while n quantifies the surface's heterogeneity or roughness, and a higher value of n corresponds to a reduction in surface roughness, whereas a lower value of n indicates increased surface roughness, with $-1 < n < 1$. For semicircles, n typically falls between 0.5 and 1.

Table 5. Effect of APMS Concentration on the EIS Parameters of XC18 Steel Corrosion in a 1 M HCl Solution at 303 K

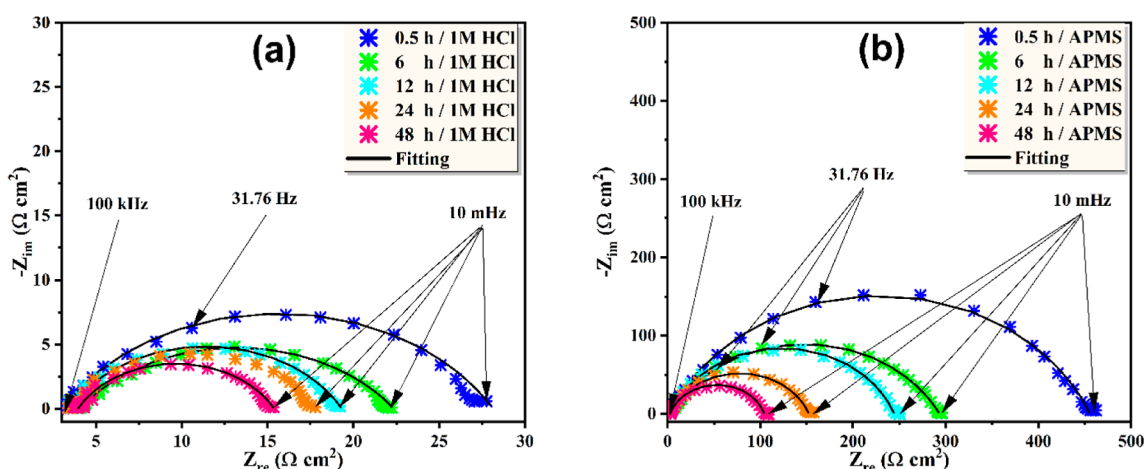| inhibitor	concentration (mol L^{-1})	R_s (Ω cm^2)	R_{ct} (Ω cm^2)	n	$Q \times 10^{-4}$ (S^n Ω^{-1} cm^{-2})	C_{dl} (μF cm^{-2})	$X^2 \times 10^{-3}$	η_{EIS} (%)
blank	1	0.14	25.01 ± 0.05	0.90 ± 0.08	1.772 ± 0.006	97	0.5	-
APMS	1 × 10^{-4}	0.16	113.52 ± 0.04	0.87 ± 0.04	0.567 ± 0.004	26	0.8	77.94
	5 × 10^{-4}	0.19	183.13 ± 0.06	0.88 ± 0.09	0.415 ± 0.008	20	0.1	86.32
	1 × 10^{-3}	0.11	259.21 ± 0.09	0.89 ± 0.10	0.254 ± 0.009	13	0.2	90.33
	5 × 10^{-3}	0.12	453.10 ± 0.07	0.84 ± 0.07	0.153 ± 0.007	6	0.2	94.47

Figure 9. Time-dependent impedance responses presented in the Nyquist plots of XC18 steel in (a) 1.0 M HCl and (b) with the presence of 5×10^{-3} M of APMS at 303 K.

Table 6. Changes in EIS Parameters with Submersion Duration for XC18 Steel with and without the Presence of 5×10^{-3} M of APMS at 303 K

| inhibitor	time (h)	R_{ct} (Ω cm^2)	n	$Q \times 10^{-4}$ (S^n Ω^{-1} cm^{-2})	C_{dl} (μF cm^2)	η_{EIS} (%)
blank	0.5	25.01 ± 0.05	0.90 ± 0.04	1.772 ± 0.006	97	–
	6	18.30 ± 0.08	0.85 ± 0.07	2.541 ± 0.008	104	–
	12	15.81 ± 0.04	0.84 ± 0.05	2.880 ± 0.003	110	–
	24	14.02 ± 0.03	0.85 ± 0.02	2.971 ± 0.004	120	–
	48	11.41 ± 0.07	0.87 ± 0.09	3.012 ± 0.008	129	–
APMS	0.5	453.10 ± 0.06	0.84 ± 0.05	0.153 ± 0.009	6	94.47
	6	290.51 ± 0.05	0.86 ± 0.04	0.233 ± 0.006	10	93.70
	12	241.32 ± 0.04	0.87 ± 0.04	0.294 ± 0.005	14	93.44
	24	149.71 ± 0.10	0.88 ± 0.09	0.452 ± 0.012	22	90.65
	48	101.42 ± 0.09	0.89 ± 0.08	0.535 ± 0.010	28	88.75
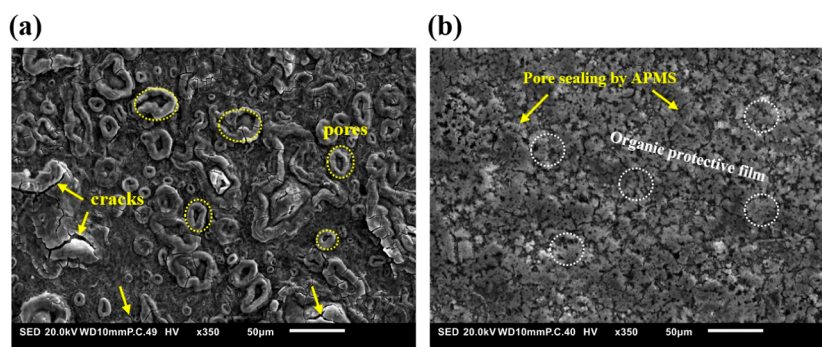
Figure 10. SEM images of XC18 steel samples after immersion in 1.0 M HCl for 48 h (a) without and (b) with $5 \times 10^{-}$ M of APMS inhibitor.

Additionally, j is used to denote the imaginary number. In the provided expression, $\omega_{max} = 2\pi f_{max}$, where f_{max} corresponds to the frequency at which Z_{Im} reaches its maximum.

The practically constant value of R_s (Table 5) indicates that the addition of APMS has no impact on the electrolytic solution's stability. Moreover, there were no notable changes in the phase shift values (n). This suggests that charge transfer acted as the primary mechanism governing XC18's dissolution in a 1 M HCl medium.[45] However, the inclusion of APMS reduces the charge accumulation over the XC18 surface, as indicated by the decreased value of Q. The inhibitor's protective capability can be assessed by examining the thickness of the electrical double layer formed upon the deposition of APMS on the XC18 surface. An increase in

thickness leads to a decrease in C_{dl}. Table 5 illustrates that with the increase of APMS doses, there is a concurrent reduction in C_{dl}. Upon closer examination of the phase angle plots (Figure 7b), at lower frequencies of Bode plots, the addition of inhibitor molecules leads to an increase in impedance modulation, indicating the formation of a protective inhibitor film on the metallic surface. Moreover, the trend of escalating phase angle values in the direction of −90°, representing a capacitive nature, suggests that inhibitors contribute to the smoothness of the metal surface by reducing the corrosion rate, suggesting enhanced inhibition efficiency.

3.4.4. EIS Evaluation for Long Time Immersion. After conducting research on temperature and concentration effects, the assessment of the corrosion performance of the protective
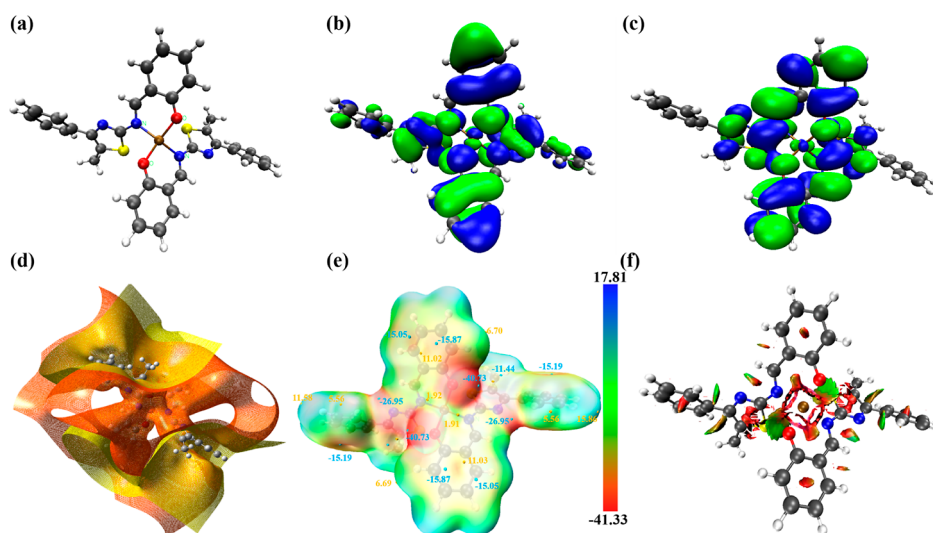
Figure 11. (a) Optimized geometry configuration, electron density distribution of the (b) HOMO and (c) LUMO orbitals, (d) ESP map, (e) ESP mapped molecular vdW surface, and (f) color-filled RDG map of the optimized configuration of the APMS molecule. (The blue region represents the formation of hydrogen bonds, the red region represents the repulsive interaction, and the green region represents the van der Waals effect.)

organic layer was performed at different immersion times. We anticipate that this factor will significantly affect the inhibition capability. The purpose of this study is to assess the stability of APMS in a corrosive environment. The investigation tracks its performance over a period of 30 min to 48 h of submersion under constant circumstances of inhibitor concentration and temperature. As the immersion duration in the acidic solution increases, Figure 9 clearly shows a trend where the sizes of the capacitive semicircles increasingly increase. The determined inhibition percentages and other pertinent characteristics derived using the EIS graphs (Figure 9) are shown in Table 6, categorized based on different immersion times. The table clearly indicates that the R_{ct} of XC18 decreases significantly with increasing immersion time, both with and without 5×10^{-3} mol L^{-1} APMS. After 48 h, the R_{ct} values are 11.41 Ω cm^2 without APMS and 101.40 Ω cm^2 with the addition of APMS.

This is primarily explained by the fact that when the metal surface comes into contact with the HCl solution, a shielding layer is formed on it. Immersion time has an impact on the creation of an APMS shielding film on the surface of XC18 in addition to the inhibitor's molecular structure. These findings show that even after extended immersion times, the inhibitor coating continues to deposit on the XC18 surface. As a result, the film's durability and ability to hinder the surface degradation process grow stronger and more efficient.[46]

3.5. Morphological Analysis. After immersion in 1 M HCl, SEM images of XC18 steel were captured after 48 h, both with and without the presence of APMS, as depicted in Figure 10. The SEM images of the smoothed XC18 sample in the acidic solution revealed a significantly damaged surface, featuring cracks, holes, and crevices, as highlighted by arrows and semicircles (Figure 10a). After 48 h of treatment process in the presence of 5×10^{-3} M of APMS inhibitor, a unique protective film of APMS grows on the XC18 surface, as depicted in Figure 10b. Such effective sealing would be attributed to the donor−acceptor character of APMS and its strong adsorption ability on the metal surface, which effectively inhibits the corrosion of XC18 steel in the 1 M HCl environment.[47] The shielding nature of this protective layer is demonstrated in the inhibition performance obtained from

the electrochemical measurements. The active adsorption of the APMS inhibitor operating the growth process of the organic layer is affected by the electron-transfer behavior and the bonding compatibility between APMS and the metal surface by electron donor−acceptor reactions, as will be proved later by DFT and DFTB calculations.

3.6. Theoretical Perspectives. The DFT approach was employed to examine the charge-transfer dynamics and inherent characteristics. Initially, an investigation was carried out using the distribution of energy levels in molecular orbitals (MOs), ESP, vdW surfaces colored according to ESP, and the noncovalent interaction (NCI) approach referred to as RDG. The objective of this analysis was to examine the intermolecular interactions involving the inhibitor molecule. Through the application of computational chemistry methods rooted in DFT, the molecular electronic attributes closely linked to the molecules' reactivity have been assessed. Within the realm of DFT calculations, the energies of frontier orbitals and descriptors of chemical reactivity serve as significant indicators, aiding in the understanding of the inhibition efficacy exhibited by organic molecules during the corrosion inhibition process of metals. Following the optimization of the APMS structure (Figure 11a), the energies of the HOMO and the LUMO were acquired, as depicted in Figure 11. Table 7

Table 7. Quantum Chemical Parameters Derived From DFT Simulation for Evaluating the Molecular Reactivity of APMS

E_{HOMO} (eV)	E_{LUMO} (eV)	IP (eV)	EA (eV)	ΔE_{gap} (eV)	χ (eV)	η (eV)	ΔN
−5.40	−2.13	5.40	2.13	3.26	3.76	1.64	0.32

presents the parameters alongside the corresponding quantum chemical values, encompassing E_{HOMO}, E_{LUMO}, ΔE_{gap}, ΔN, χ, and additional parameters. Initially, the frontier molecular orbital (FMO) theory was employed to assess the reactivity and arrangement of molecular orbitals within the inhibitor. The interfacial interaction between APMS and the XC18 surface can be largely anticipated through analysis of HOMO and LUMO energies. E_{LUMO} signifies the ability of the APMS
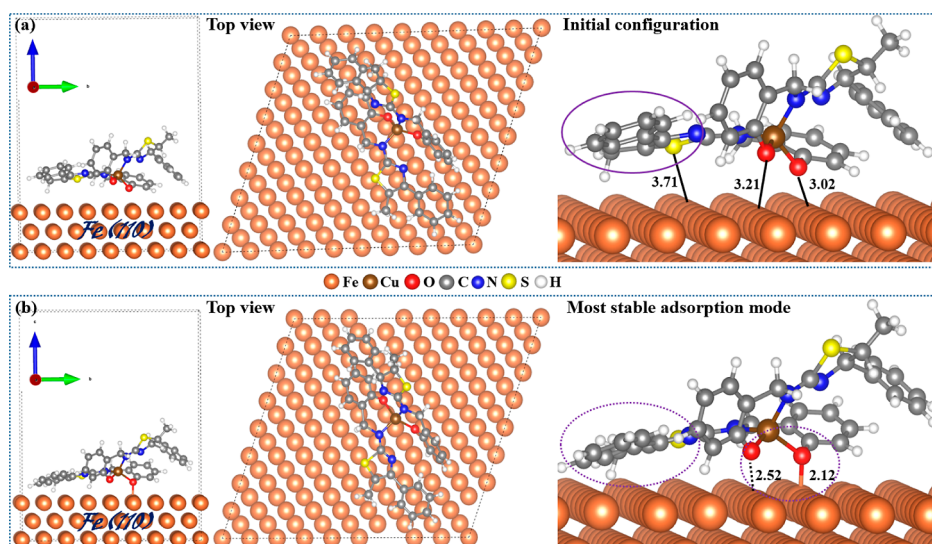
Figure 12. Computational insights into the adsorption mechanism between APMS and the XC18 surface. (a) Adsorption mode with the precalculation position and (b) most stable adsorption configuration of the APMS molecule onto the Fe(110) surface: top and side views.

molecule to accept electrons, while E_{HOMO} indicates the molecule's chemical reactivity for donating electrons.[48−50] As depicted in Figure 11b, HOMO spans across the entirety of the APMS molecule, encompassing all of its regions. Conversely, the LUMO extends over the entire APMS molecule with the exception of two benzene rings (Figure 11c). The APMS inhibitor displays a notably low chemical hardness (η) value, as indicated in Table 7. This characteristic suggests that the examined APMS compound holds the potential to effectively inhibit the corrosion of XC18.[51] Further, as observed in Table 7, the investigated inhibitor demonstrated a positive ΔN value that falls below 3.6. This observation implies that the APMS compound donates its electrons to the steel surface.[36] The energy gap (ΔE_{gap}), along with E_{HOMO} and E_{LUMO}, is essential in dictating the adsorption of molecules onto metallic surfaces. ΔE_{gap} signifies the APMS responsiveness to the XC18 surface. As ΔE_{gap} diminishes, the inhibitor's reactivity naturally intensifies, leading to an augmented adsorption onto the metallic surface.[52] The E_{HOMO} of APMS (−5.40 eV) closely aligns with the Fermi level of iron (−5.17 eV), more so than the E_{LUMO} (−2.13 eV). Moreover, the disparity in energy between APMS's E_{HOMO} and the iron Fermi level is −0.23 eV, underscoring the charge-transfer behavior of APMS.[53]

The electrostatic potential (ESP) is a scalar field that describes the electrostatic interactions within a molecular system. ESP provides insights into the charge distribution and polarity of a molecule. The ESP surface (depicted in Figure 11d) represents the distance at which a positively charged test particle encounters specific attraction or repulsion interactions with the synthesized molecule.[54] Positive ESP values indicate regions where electron density is low (positively charged), while negative ESP values indicate regions with higher electron density (negatively charged). ESP is used to analyze and predict various molecular properties, including reactivity and intermolecular interactions. Figure 11d illustrates the three-dimensional representations of ESP for APMS. The ESP reveals regions of negative ESP (highlighted in shades of red), which are prominently concentrated across the molecule, excluding the hydrogen atoms within the rings. While regions of positive ESP are visualized as a distinctive yellowish mass.

To enhance the understanding of intermolecular interactions and forecast nucleophilic and electrophilic attacks, the disposition of the ESP on the van der Waals surface was carried out. It is recognized that regions with more negative ESP (depicted in red) and more positive ESP (depicted in blue) signify electrophilic and nucleophilic reactivity, respectively. Additionally, areas marked with orange and blue dots on the vdW surface correspond to the ESP maxima and minima, respectively. Hence, as depicted in Figure 11e, it becomes evident that the regions of negative isosurfaces and the points of minimum ESP are primarily situated around sulfur atoms and the electron pairs of nitrogen and oxygen atoms. This observation indicates the potential of these areas to function as centers for nucleophilic reactions when the interaction occurs between the APMS inhibitor and the unoccupied orbital of iron (Fe). Indeed, the sulfur atoms located within the thiazole groups displayed the most pronounced negative potential (indicating the lowest value on the global surface) with an ESP value of −40.73 kcal mol⁻¹. Following this, the nitrogen atoms within the thiazole groups exhibited an ESP value of −26.95 kcal mol⁻¹. These results underscore the significance of the delocalized electrons within the thiazole groups, underscoring their pivotal role in primary bonding and electron charge transfer from the APMS to the XC18 surface. These electron-rich areas can function as donors and acceptors for intermolecular interactions. While FMO has found widespread application in assessing the overall reactivity characteristics of organic molecules, it falls short of adequately capturing the localized electronic attributes within molecules due to its reliance on delocalized molecular orbitals. Consequently, RDG analysis was conducted to visually assess the intermolecular interactions, as depicted in Figure 11f. The NCI concept is a good theoretical framework used to clarify intermolecular interactions and assess the attributes of faint connections within molecular systems. In this color-filled RDG isosurface, the presence of red and green colors corresponds to repulsive and vdW interactions, respectively (Figure 11f).[53] As illustrated in Figure 11f, vdW interactions exist between oxygen and sulfur atoms as well as between nitrogen and hydrogen atoms. These interactions contribute to the stability

of the APMS complex. Moreover, steric effects are also located at the centers of the rings.

To acquire a deeper comprehension of how the APMS molecule interacts with the Fe surface, we carried out first-principles DFTB calculations. These calculations involved a setup in which an APMS inhibitor was deposited onto the Fe(110) surface plane. Prior to any optimization, the APMS inhibitor was placed at discrete locations, showcasing an initial surface distance of $d_{O-Fe} = 3.02$ and $d_{S-Fe} = 3.71$ Å, as clearly demonstrated in Figure 12a (side view). Furthermore, we determined the adsorption energy using eq 7. Figure 12b illustrates that when the APMS molecule adopts a nearly parallel orientation (O contact), it adheres to the Fe surface in an almost planar configuration. In this arrangement, the polar groups and the π-bonds of the aromatic ring engage in direct chemisorptive interactions with the Fe surface. Compared to the initial adsorption configuration of APMS on the Fe surface, the APMS molecule establishes a connection with the Fe surface through its active sites. This suggests that the presence of active heteroatoms promotes such interfacial behavior, leading to strong interactions with the surface. Moreover, the findings unambiguously show that the APMS−Fe bond distances measure around 2.12 and 2.52 Å when taken from the O atoms of the adsorbed APMS on the Fe surface, confirming the robust adsorption of the APMS inhibitor molecule. Indeed, in the most stable adsorption configuration, the formation of chemical bonds was favored due to the fact that the covalent radii of the bonded atoms O and Fe fall within the sum of the covalent radii of O and Fe (the sum of the oxygen radius, $r(O)$, and the iron radius, $r(Fe)$, equals 1.98 Å).[53] In comparison to the initial configuration, the APMS inhibitor forms a notably more stable protective layer on the Fe(110) surface, leading to considerably increased stability with an adsorption energy of −5.12 eV (Figure 12b). The preceding findings demonstrate that the APMS inhibitor aligns with the high electron localization characteristics observed in the bonding regions, as previously discussed through the ESP-mapped molecular vdW surface. Consequently, the electrons residing within the active sites and the polar groups of the inhibitor molecule were moved to the vacant d orbitals of the Fe atom, enhancing both the effectiveness of binding and the transfer of the electronic charge from APMS to the Fe surface.

3.7. Comparative Analysis with Other SB Derivatives in Some Previous Studies. Table 8 provides a comparative analysis of the inhibition effectiveness of the current organic inhibitor alongside previous studies involving protective techniques employing Schiff bases for steel alloys. The inhibition performance of the APMS-based inhibitor, exceeding 94%, seems to surpass the conventional threshold. This is due to the robustness of the protective structure, where the APMS compound fills in the microdefects on the surface of XC18 steel. The present study revealed the development of strong coordination bonds between APMS and the steel surface, occurring in a simultaneous adsorption mode characterized by the formation of covalent bonds. Consequently, the protective organic structure formed by APMS on the XC18 surface significantly enhances both chemical reliability and corrosion resistance.

3.8. APMS/Surface Interaction Mechanism. Based on experimental findings and theoretical computations, Figure 13 illustrates the corrosion inhibition mechanism of the APMS inhibitor. Considering thermodynamic and theoretical results, the adsorption of APMS occurs through two main mechanisms: physical and chemical. Understanding the adsorption mechanism is challenging because inhibitors bond to surfaces in two ways: physically and chemically. For APMS, it is probable that the molecules adhere to the surface of the XC18 steel through vdW forces and covalent bonds. The chemical adsorption on the XC18 steel surface is elucidated by the donor−acceptor interaction, where the charges of donating O and S atoms and π-electrons of APMS bind with the empty d-orbitals of Fe atoms. Additionally, electrons jump from the iron atoms to the APMS's rings, filling its empty π-antibonding orbitals through a back-donation mechanism. This process, in turn, enhances the adsorption of APMS on the XC18 surface.[56] Furthermore, the introduction of metal complexes as compound corrosion inhibitors facilitated the bonding of APMS molecules through intermolecular interactions. This interaction, in turn, promoted the bonding of more atoms to the surface of Fe. Consequently, the coadsorption of APMS-based inhibitors resulted in the formation of a more robust and condensed shield on the metal surface. Thus, APMS synergistically achieves a notable drop in the degree of corrosion of XC18 steel.

4. CONCLUSIONS

Through experimental assessments and contemporary theoretical chemistry principles, we elucidated the corrosion inhibition mechanism of APMS as a copper(II) complex of an SB inhibitor on the XC18 surface in a HCl solution. The superior anticorrosion performance of APMS was provided by its electron-donor and electron-acceptor characteristics. The enhanced performance was attributed to its electron donor−acceptor attributes. The electrochemical findings demonstrated that the adsorption of APMS changed the surface of the XC18 steel, promoting the development of an organic layer. Irrespective of the employed method, the corrosion inhibition effectiveness of XC18 increased at a higher APMS concentration. The synergistic mechanism and interfacial adsorption behavior of the APMS inhibitor were thoroughly explored through quantum chemical calculations (RDG, ESP, and ESP on vdW molecular surface) and first-principles DFTB simulations, which assess both inter- and intramolecular interaction contributions. Regarding the mechanism behind the formation of the organic film, it is possible that the APMS inhibitor adheres to the XC18 surface through a significant synergistic inhibition effect on the corrosion of XC18 steel. This process likely includes the transfer of electrons between the heteroatoms and the XC18 surface. Strong covalent bond

Table 8. Comparative Analysis of the Inhibition Performance of APMS and the Previously Studied SB Derivatives

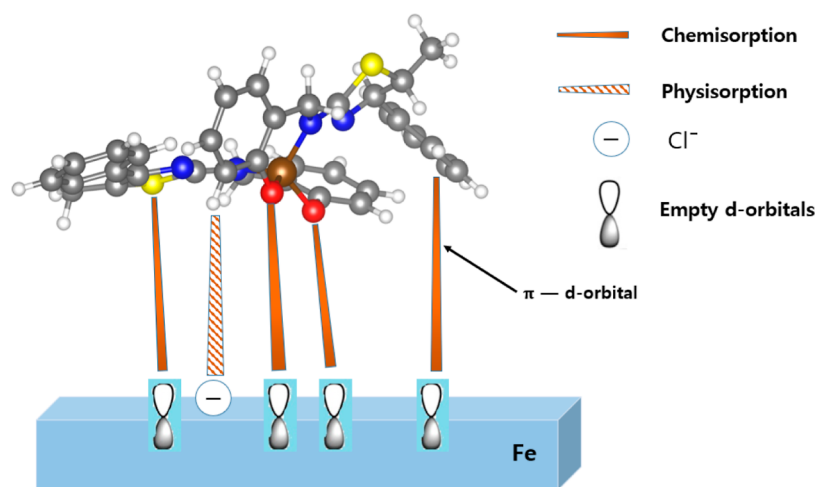| SB derivatives	steel alloy	optimum concentration	IE % (from EIS)	ref
diazene-based SB	X65 steel	100 ppm	92.40	4
6-SH	carbon steel	3×10^{-3} mol L^{-1}	94.29	55
PBPE	mild steel	800 mg L^{-1}	85.39	56
CMPMA	mild steel	300 ppm	91.99	57
PMAD	carbon steel	2×10^{-3} mol L^{-1}	83.42	58
PBPM3	mild steel	800 mg L^{-1}	83.92	47
APMS	XC18 steel	5×10^{-3} mol L^{-1}	94.47	current work

Figure 13. Facile and rapid formation of the organic layer of APMS. Influence on charge-transfer behavior and interaction with corrosive solution.

formation occurred in a nearly parallel adsorption configuration as revealed by DFTB calculations.

ASSOCIATED CONTENT

Data Availability Statement

The data related to this work can be obtained from the corresponding authors upon reasonable request.

AUTHOR INFORMATION

Corresponding Authors

    Abdelkarim Chaouiki − *Materials Electrochemistry Laboratory, School of Materials Science and Engineering, Yeungnam University, Gyeongsan 38541, Republic of Korea;* ⊙ orcid.org/0000-0003-0622-8746; Email: abdelkarim.chaouiki@yu.ac.kr

    Maryam Chafiq − *Materials Electrochemistry Laboratory, School of Materials Science and Engineering, Yeungnam University, Gyeongsan 38541, Republic of Korea;* Email: maryam.chafiq@yu.ac.kr

    Young Gun Ko − *Materials Electrochemistry Laboratory, School of Materials Science and Engineering, Yeungnam University, Gyeongsan 38541, Republic of Korea;* Email: younggun@ynu.ac.kr

Authors

    Hamid Ahchouch − *Laboratory of Applied Chemistry and Environment, ENSA, University Ibn Zohr, Agadir 80000, Morocco*

    Aisha H. Al-Moubaraki − *Department of Chemistry, Faculty of Sciences-Alfaisaliah Campus, University of Jeddah, Jeddah 21589, Saudi Arabia*

    Jamilah M. Al-Ahmari − *Department of Chemistry, Faculty of Sciences-Alfaisaliah Campus, University of Jeddah, Jeddah 21589, Saudi Arabia*

    Azza A. Al-Ghamdi − *Department of Chemistry, Faculty of Sciences-Alfaisaliah Campus, University of Jeddah, Jeddah 21589, Saudi Arabia*

    Lahcen Bammou − *Laboratory of Applied Chemistry and Environment, ENSA, University Ibn Zohr, Agadir 80000, Morocco; Higher School of Education and Training, Agadir 80000, Morocco*

    M'hammed Belkhaouda − *Laboratory of Applied Chemistry and Environment, ENSA, University Ibn Zohr, Agadir 80000, Morocco; Laboratory of Sciences and Didactic of Sciences, CRMEF, Inzegane 80000, Morocco*

Complete contact information is available at:
https://pubs.acs.org/10.1021/acsomega.3c09097

Author Contributions

Hamid Ahchouch: Conceptualization, methodology, investigation, writing − original draft, and writing − review and editing. **Abdelkarim Chaouiki:** Conceptualization, investigation, computational calculation, visualization, writing − original draft, writing − review and editing, and supervision. **Aisha H. Al-Moubaraki:** Investigation, formal analysis, and funding acquisition. **Jamilah M. Al-Ahmari:** Investigation, data curation, and funding acquisition. **Azza A. Al-Ghamdi:** Investigation, formal analysis, and funding acquisition. Lahcen Bammou and **M'hammed Belkhaouda:** Visualization and formal analysis. **Maryam Chafiq:** Data curation, writing − original draft, and writing − review and editing. **Young Gun Ko:** Funding acquisition, review, and editing.

Notes

The authors declare no competing financial interest.

ACKNOWLEDGMENTS

REFERENCES

(1) Shetty, P. Schiff Bases: An Overview of Their Corrosion Inhibition Activity in Acid Media against Mild Steel. *Chem. Eng. Commun.* **2020**, *207* (7), 985−1029.

(2) Salim, R.; Ech-chihbi, E.; Oudda, H.; El Hajjaji, F.; Taleb, M.; Jodeh, S. A Review on the Assessment of Imidazo[1,2-a]Pyridines As Corrosion Inhibitor of Metals. *J. Bio Tribo Corros.* **2019**, *5* (1), 14.

(3) Panda, A. K.; Purohit, A. K.; Upadhyay, A.; Sahoo, M. K.; Kar, P. K. Corrosion Inhibition Studies on Mild Steel in HCl by a Newly Synthesized Benzil Monohydrazone Based Schiff Base. *J. Indian Chem. Soc.* **2021**, *98* (12), 100245.

(4) A Altalhi, A. Anticorrosion Investigation of New Diazene-Based Schiff Base Derivatives as Safe Corrosion Inhibitors for API X65 Steel Pipelines in Acidic Oilfield Formation Water: Synthesis, Experimental, and Computational Studies. *ACS Omega* **2023**, *8* (34), 31271−31280.

(5) Chaouiki, A.; Chafiq, M.; Rbaa, M.; Salghi, R.; Lakhrissi, B.; Ali, I. H.; Bashir, S.; Chung, I.-M. Comprehensive Assessment of Corrosion Inhibition Mechanisms of Novel Benzimidazole Compounds for Mild Steel in HCl: An Experimental and Theoretical Investigation. *J. Mol. Liq.* **2020**, *320*, 114383.

(6) Jia, Y.; Li, J. Molecular Assembly of Schiff Base Interactions: Construction and Application. *Chem. Rev.* **2015**, *115* (3), 1597−1621.

(7) Jayaseelan, P.; Prasad, S.; Vedanayaki, S.; Rajavel, R. Synthesis, Characterization, Anti-Microbial, DNA Binding and Cleavage Studies of Schiff Base Metal Complexes. *Ar. J. Chem.* **2016**, *9*, S668−S677.

(8) Al-Amiery, A.; Shaker, L. M.; Betti, N. Experimental Studies on the Inhibition Performances of Isatine Schiff Base for the Corrosion of Mild Steel in Hydrochloric Acid. *Mater. Today: Proc.* **2022**, *56*, 2209−2212.

(9) Uddin, M. N.; Ahmed, S. S.; Alam, S. M. R. REVIEW: Biomedical Applications of Schiff Base Metal Complexes. *J. Coord. Chem.* **2020**, *73* (23), 3109−3149.

(10) Boulechfar, C.; Ferkous, H.; Delimi, A.; Berredjem, M.; Kahlouche, A.; Madaci, A.; Djellali, S.; Boufas, S.; Djedouani, A.; Errachid, A.; Ali Khan, A.; Boublia, A.; Lemaoui, T.; Benguerba, Y. Corrosion Inhibition of Schiff Base and Their Metal Complexes with [Mn (II), Co (II) and Zn (II)]: Experimental and Quantum Chemical Studies. *J. Mol. Liq.* **2023**, *378*, 121637.

(11) Boukazoula, S.; Haffar, D.; Bourzami, R.; Toukal, L.; Dorcet, V. Synthesis, Characterizations, Crystal Structure, Inhibition Effects and Theoretical Study of Novel Schiff Base on the Corrosion of Carbon Steel in 1 M HCl. *J. Mol. Struct.* **2022**, *1261*, 132852.

(12) Sayed, F. N.; Ashmawy, A. M.; Saad, S. M.; Omar, M. M.; Mohamed, G. G. Design, Spectroscopic Characterization, DFT, Molecular Docking, and Different Applications: Anti-Corrosion and Antioxidant of Novel Metal Complexes Derived from Ofloxacin-Based Schiff Base. *J. Organomet. Chem.* **2023**, *993*, 122698.

(13) El-Lateef, H. M. A.; Soliman, K. A.; Al-Omair, M. A.; Adam, M. S. S. A Combination of Modeling and Experimental Approaches to Investigate the Novel Nicotinohydrazone Schiff Base and Its Complexes with Zn(II) and ZrO(II) as Inhibitors for Mild-Steel Corrosion in Molar HCl. *J. Taiwan Inst. Chem. Eng.* **2021**, *120*, 391−408.

(14) Arshad, I.; Qureshi, K.; Saleemi, A. S.; Abdullah, A.; Bahajjaj, A. A. A.; Ali, S.; Bokhari, A. Melamine-Isatin Tris Schiff Base as an Efficient Corrosion Inhibitor for Mild Steel in 0.5 Molar Hydrochloric Acid Solution: Weight Loss, Electrochemical and Surface Studies. *RSC Adv.* **2023**, *13* (28), 19301−19311.

(15) Abd-elmaksoud, G. A.; Abusaif, M. S.; Ammar, Y. A.; Al-Sharbasy, S.; Migahed, M. A. Construction, Characterization, DFT Computational Study, and Evaluation the Performance of Some New N-Amino Pyridinone Schiff Base Catalyzed with Ceric(IV) Ammonium Nitrate (CAN) as Corrosion Inhibitors in Some Petroleum Applications. *Arab. J. Sci. Eng.* **2023**, *48* (12), 16167−16185.

(16) Liu, Y.; Feng, H.; Wang, L.; Yang, T.; Qiu, J. Preparation of Bis-Thiophene Schiff Alkali-Copper Metal Complex for Metal Corrosion Inhibition. *Materials* **2023**, *16* (8), 3214.

(17) Thabet, H. K.; AlGhamdi, J. M.; Mohammed, H. A.; Elsaid, M. A. M.; Ashmawy, A. M. Anticorrosion Agents for Carbon Steel in Acidic Environments: Synthesis and Quantum Chemical Analysis of New Schiff Base Compounds with Benzylidene. *ACS Omega* **2023**, *8* (42), 39770−39782.

(18) Zobeidi, A.; Neghmouche Nacer, S.; Atia, S.; Kribaa, L.; Kerassa, A.; Kamarchou, A.; AlNoaimi, M.; Ghernaout, D.; Ali, M. A.; Lagum, A. A.; Elboughdiri, N. Corrosion Inhibition of Azo Compounds Derived from Schiff Bases on Mild Steel (XC70) in (HCl, 1 M DMSO) Medium: An Experimental and Theoretical Study. *ACS Omega* **2023**, *8* (24), 21571−21584.

(19) Abd-Elzaher, M. M.; Labib, A. A.; Mousa, H. A.; Moustafa, S. A.; Ali, M. M.; El-Rashedy, A. A. Synthesis, Anticancer Activity and Molecular Docking Study of Schiff Base Complexes Containing Thiazole Moiety. *Beni-Suef Univ. J. Basic Appl. Sci.* **2016**, *5* (1), 85−96.

(20) Ahchouch, H.; El House, M.; Al-Moubaraki, A. H.; Noor, E. A.; Hadfi, A.; Driouiche, A.; Bammou, L.; Belkhaouda, M.; Salghi, R.; Chafiq, M.; Chaouiki, A.; Ko, Y. G. From Nature to Protection: Unleashing the Protective Potential of Hedera Helix Leaves against Corrosion in Harsh Acidic Environments Using Experimental and Theoretical Insights. *Ar. J. Chem.* **2024**, *17* (2), 105593.

(21) Chafiq, M.; Chaouiki, A.; Suhartono, T.; Hazmatulhaq, F.; Ko, Y. G. Interface Engineering of LDH-Based Material as Efficient Anti-Corrosive System via Synergetic Performance of Host, Interlayers, and Morphological Features of Nature-Mimic Architectures. *Chem. Eng. J.* **2023**, *462*, 142239.

(22) Chaouiki, A.; Chafiq, M.; Suhartono, T.; Ko, Y. G. Unveiling the In-Situ Formation Mechanism of Nano-Fir Tree-like Architecture: Yolk-Shell Structure Enables the Development of an Advanced Multifunctional Template. *Chem. Eng. J.* **2023**, *470*, 144355.

(23) Chaouiki, A.; In Han, D.; Ko, Y. G. Computational Molecular-Level Prediction of Heterocyclic Compound-Metal Surface Interfacial Behavior. *J. Colloid Interface Sci.* **2022**, *622*, 452−468.

(24) Chaouiki, A.; Chafiq, M.; Al-Moubaraki, A. H.; Bakhouch, M.; El Yazidi, M.; Ko, Y. G. Electrochemical Behavior and Interfacial Bonding Mechanism of New Synthesized Carbocyclic Inhibitor for Exceptional Corrosion Resistance of Steel Alloy: DFTB, MD and Experimental Approaches. *Ar. J. Chem.* **2022**, *15* (12), 104323.

(25) Chaouiki, A.; Hazmatulhaq, F.; Han, D. I.; Al-Moubaraki, A. H.; Bakhouch, M.; Ko, Y. G. Predicting the Interaction between Organic Layer and Metal Substrate through DFTB and Electrochemical Approach for Excellent Corrosion Protection. *J. Ind. Eng. Chem.* **2022**, *114*, 190−204.

(26) Al-Moubaraki, A. H.; Chaouiki, A.; Alahmari, J. M.; Al-Hammadi, W. A.; Noor, E. A.; Al-Ghamdi, A. A.; Ko, Y. G. Development of Natural Plant Extracts as Sustainable Inhibitors for Efficient Protection of Mild Steel: Experimental and First-Principles Multi-Level Computational Methods. *Materials* **2022**, *15* (23), 8688.

(27) Chafiq, M.; Chaouiki, A.; Salghi, R.; Ko, Y. G. Fabrication of Branch-like Aph@ LDH-MgO Material through Organic-Inorganic Hybrid Conjugation for Excellent Anti-Corrosion Performance. *J. Magnesium Alloys* **2023**, *11* (7), 2469−2485.

(28) Lgaz, H.; Chaouiki, A.; Chafiq, M.; Salghi, R.; Tachallait, H.; Bougrin, K.; Chi, H.-Y.; Kwon, C.; Chung, I.-M. Evaluating the Corrosion Inhibition Properties of Novel 1,2,3-Triazolyl Nucleosides and Their Synergistic Effect with Iodide Ions against Mild Steel Corrosion in HCl: A Combined Experimental and Computational Exploration. *J. Mol. Liq.* **2021**, *338*, 116522.

(29) Hsissou, R.; Benhiba, F.; El Aboubi, M.; Abbout, S.; Benzekri, Z.; Safi, Z.; Rafik, M.; Bahaj, H.; Kaba, M.; Galai, M.; Wazzan, N.; Briche, S.; Boukhris, S.; Zarrouk, A.; EbnTouhami, M.; Rafik, M. Synthesis and Performance of Two Ecofriendly Epoxy Resins as a Highly Efficient Corrosion Inhibition for Carbon Steel in 1 M HCl Solution: DFT, RDF, FFV and MD Approaches. *Chem. Phys. Lett.* **2022**, *806*, 139995.

(30) Zehra, B. F.; Said, A.; Eddine, H. M.; Hamid, E.; Najat, H.; Rachid, N.; Toumert, L. I. Crataegus Oxyacantha Leaves Extract for Carbon Steel Protection against Corrosion in 1M HCl: Characterization, Electrochemical, Theoretical Research, and Surface Analysis. *J. Mol. Struct.* **2022**, *1259*, 132737.

(31) Al Kiey, S. A.; Hasanin, M. S.; Dacrory, S. Potential Anticorrosive Performance of Green and Sustainable Inhibitor Based on Cellulose Derivatives for Carbon Steel. *J. Mol. Liq.* **2021**, *338*, 116604.

(32) Kesari, P.; Udayabhanu, G.; Roy, A.; Pal, S. Chitosan Based Titanium and Iron Oxide Hybrid Bio-Polymeric Nanocomposites as Potential Corrosion Inhibitor for Mild Steel in Acidic Medium. *Int. J. Biol. Macromol.* **2023**, *225*, 1323−1349.

(33) Noor, E. A.; Al-Moubaraki, A. H.; Al-Masoudi, D. I.; Chafiq, M.; Chaouiki, A.; Ko, Y. G. Corrosion Behavior of Carbon Steel X36 in Solutions of Soils Collected from Different Areas Linked to the Main Pipe Network of a Water Distribution System in Jeddah City. *Metals* **2023**, *13* (4), 670.

(34) Wang, Q.; Zhang, Q.; Liu, L.; Zheng, H.; Wu, X.; Li, Z.; Gao, P.; Sun, Y.; Yan, Z.; Li, X. Experimental, DFT and MD Evaluation of Nandina Domestica Thunb. Extract as Green Inhibitor for Carbon Steel Corrosion in Acidic Medium. *J. Mol. Struct.* **2022**, *1265*, 133367.

(35) Saha, S. Kr.; Murmu, M.; Murmu, N. C.; Banerjee, P. Benzothiazolylhydrazine Azomethine Derivatives for Efficient Corrosion Inhibition of Mild Steel in Acidic Environment: Integrated Experimental and Density Functional Theory Cum Molecular Dynamics Simulation Approach. *J. Mol. Liq.* **2022**, *364*, 120033.

(36) Quraishi, M. A.; Chauhan, D. S.; Saji, V. S. *Heterocyclic Organic Corrosion Inhibitors: Principles and Applications*; Elsevier: Amsterdam, Netherlands ; Cambridge, MA, 2020.

(37) Choudhary, S.; Garg, A.; Mondal, K. Relation Between Open Circuit Potential and Polarization Resistance with Rust and Corrosion Monitoring of Mild Steel. *J. Mater. Eng. Perform.* **2016**, *25* (7), 2969−2976.

(38) Karimi, S.; Rezaeivala, M.; Sayin, K.; Tuzun, B. Experimental and Computational Investigation of 3,5-Di-Tert-Butyl-2-(((3-((2-Morpholinoethyl)(Pyridin-2-Ylmethyl) Amino)Propyl)Imino) Methyl)Phenol and Related Reduced Form as an Inhibitor for C-Steel. *Mater. Chem. Phys.* **2022**, *287*, 126152.

(39) Gao, B.; Zhang, X.; Sheng, Y. Studies on Preparing and Corrosion Inhibition Behaviour of Quaternized Polyethyleneimine for Low Carbon Steel in Sulfuric Acid. *Mater. Chem. Phys.* **2008**, *108* (2−3), 375−381.

(40) Xu, Z.; Tan, B.; Zhang, S.; Chen, J.; Li, W. Exploring of an Ecological Corrosion Inhibitor of Wood Hibiscus Leaf Extract for the Cu/H2SO4 System Based on Experimental Study and Theoretical Calculations. *J. Taiwan Inst. Chem. Eng.* **2023**, *143*, 104686.

(41) Silva, M. V. L. D.; Policarpi, E. D. B.; Spinelli, A. Syzygium Cumini Leaf Extract as an Eco-Friendly Corrosion Inhibitor for Carbon Steel in Acidic Medium. *J. Taiwan Inst. Chem. Eng.* **2021**, *129*, 342−349.

(42) Elaryian, H. M.; Bedair, M. A.; Bedair, A. H.; Aboushahba, R. M.; Fouda, A. E.-A. S. Synthesis, Characterization of Novel Coumarin Dyes as Corrosion Inhibitors for Mild Steel in Acidic Environment: Experimental, Theoretical, and Biological Studies. *J. Mol. Liq.* **2022**, *346*, 118310.

(43) Mobin, M.; Rizvi, M. Adsorption and Corrosion Inhibition Behavior of Hydroxyethyl Cellulose and Synergistic Surfactants Additives for Carbon Steel in 1 M HCl. *Carbohydr. Polym.* **2017**, *156*, 202−214.

(44) Kalkhambkar, A. G.; S K, R.; Manjanna, J.; Malimath, G. H. Effect of Expired Doxofylline Drug on Corrosion Protection of Soft Steel in 1 M HCl: Electrochemical, Quantum Chemical and Synergistic Effect Studies. *J. Indian Chem. Soc.* **2022**, *99* (9), 100639.

(45) Thakur, A.; Kaya, S.; Abousalem, A. S.; Sharma, S.; Ganjoo, R.; Assad, H.; Kumar, A. Computational and Experimental Studies on the Corrosion Inhibition Performance of an Aerial Extract of Cnicus Benedictus Weed on the Acidic Corrosion of Mild Steel. *Process Saf. Environ. Prot.* **2022**, *161*, 801−818.

(46) Chafiq, M.; Chaouiki, A.; Salghi, R.; Tachallait, H.; Bougrin, K.; Ali, I. H.; Siaj, M. Adsorption Mechanism of 3-(1,4-Disubstituted-1,2,3-Triazolyl) Uridine Nucleosides against the Corrosion of Mild Steel in HCl. *Mater. Chem. Phys.* **2021**, *268*, 124742.

(47) Li, X.-L.; Xie, B.; Lai, C.; Feng, J.-S.; Liu, X.-Q.; Chen, L.; Yang, Y.-G.; Ji, R.-W.; He, J.-Y.; Li, W.; Liu, M.-N. Adsorption and Corrosion Inhibition Performance of Two Planar Rigid Pyridine-carboxaldehyde-Based Double Schiff Bases for Mild Steel in HCl Solution: Experimental and Computational Investigations. *J. Mol. Liq.* **2022**, *355*, 118926.

(48) Hazmatulhaq, F.; Sheng, Y.; Suhartono, T.; Fatimah, S.; Chafiq, M.; Chaouiki, A.; Ko, Y. G. Electrochemical Response and Adsorption Behavior of Sulfocarbanilide Inhibitor on Oxide Layer Produced by Pulsed Plasma Electrolysis (PPE): Experimental and DFT Perspective. *Corros. Sci.* **2024**, *229*, 111849.

(49) Hazmatulhaq, F.; Suhartono, T.; Sheng, Y.; Kamil, M. P.; Chaouiki, A.; Ko, Y. G. Amelioration of 2D Hybrid Architecture for Protective Surface Using Thiourea-Based Inhibitor: Electrochemical and Computational Perspectives. *Sustainable Mater. Technol.* **2023**, *38*, No. e00757.

(50) Chaouiki, A.; Chafiq, M.; Ko, Y. G. Nature-Inspired Architecture Combining Organic-Inorganic Frameworks: Unique Structure and Active Sites toward a Stable Anti-Corrosion Coating. *Appl. Mater. Today* **2023**, *32*, 101852.

(51) Zakaria, K.; Abbas, M. A.; Bedair, M. A. Herbal Expired Drug Bearing Glycosides and Polysaccharides Moieties as Green and Cost-Effective Oilfield Corrosion Inhibitor: Electrochemical and Computational Studies. *J. Mol. Liq.* **2022**, *352*, 118689.

(52) Saha, S. Kr.; Banerjee, P. A Theoretical Approach to Understand the Inhibition Mechanism of Steel Corrosion with Two Aminobenzonitrile Inhibitors. *RSC Adv.* **2015**, *5* (87), 71120−71130.

(53) Ahchouch, H.; Chaouiki, A.; Ait Talhajt, S.; Bammou, L.; Belkhaouda, M.; Salghi, R.; Ko, Y. G. Inter- and Intra-Molecular Synergism in Designing MgO-MCC Composite-Based Coating: An Efficient Inhibitor for Excellent Anticorrosion Performance. *Process Saf. Environ. Prot.* **2023**, *177*, 1461−1476.

(54) Hasan, M. S.; Liton, A. K.; Haque, T.; Ali, M. I.; Akter, S. An Experimental and DFT Computational Study on Methyl 3-Acetyl-2-Oxo-2H-Chromene-6-Carboxylate. *Mol. Phys.* **2022**, *120* (14), No. e2103468.

(55) Jafari, H.; Ameri, E.; Hassan Vakili, M.; Berisha, A. Effect of OH Position on Adsorption Behavior of Schiff-Base Derivatives in Corrosion Inhibition of Carbon Steel in 1 M HCl. *Electrochem. Commun.* **2024**, *159*, 107653.

(56) He, J.; Li, X.; Xie, B.; He, Y.; Lai, C.; Dou, B.; Feng, J.; Liu, M.; Ji, R.; Zhao, W. Exploration of Rigid Double Schiff Base with a Symmetrical Plane as Highly Effective Corrosion Inhibitor for Mild Steel in Hydrochloric Acid Environment: Experimental and Theoretical Approaches. *Mater. Chem. Phys.* **2024**, *313*, 128785.

(57) Khanna, R.; Kalia, V.; Kumar, R.; Kumar, R.; Kumar, P.; Dahiya, H.; Pahuja, P.; Jhaa, G.; Kumar, H. Synergistic Experimental and Computational Approaches for Evaluating Pyrazole Schiff Bases as Corrosion Inhibitor for Mild Steel in Acidic Medium. *J. Mol. Struct.* **2024**, *1297*, 136845.

(58) Jafari, H.; Ameri, E.; Vakili, M. H.; Berisha, A. Novel Silicon-Based Schiff-Base as Corrosion Inhibitor for Anti-Corrosion Behavior of API 5L Grade B in 1M HCl. *Mater. Chem. Phys.* **2024**, *311*, 128499.